(V/V) was obtained from ADWIC Company for chemicals, Egypt)All compounds were used exactly as supplied, with no further purification.

2.2 Synthesis of Chs-Pyr polymer

In 100 mL of glacial acetic acid, the chitosan polymer (1.0 g) was dissolved to prepare and was stirred for 30 minutes at room temperature to form chitosan gel. After this, pyridoxal aldehyde was added dropwise (0.3g in 20ml DMF) while stirring for 30 minutes. Then the temperature was raised to 100 °C for 6 hours, Scheme 1. Petri dishes were coated with Chs-Pyr polymer hydrogel, and the solvent evaporated at room temperature.

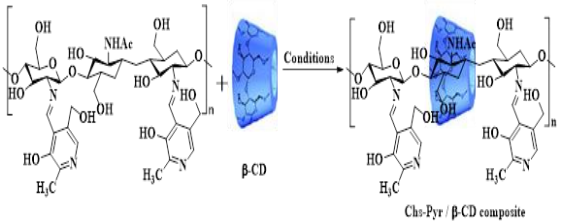

Scheme 1. Synthesis of Chs-Pyr polymer

2.3 Synthesis of pseudopolyrotaxane (Chs-Pyr/ β-CD)

Chs-Pyr polymer (1.0 g) and β-CD (3g) were mixed in DMF (25ml) at room temperature for 18 hours to form the inclusion complex, Scheme 2. It was obtained in the form of faint yellow powder after the precipitate was filtered out under a vacuum and dried at room temperature.

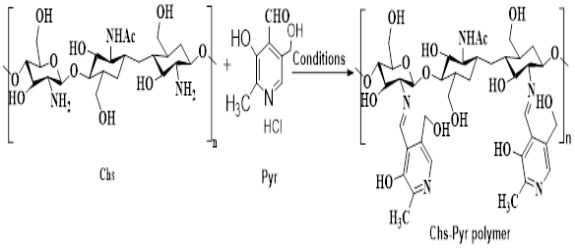

Scheme 2. Synthesis of of pseudopolyrotaxane (Chs-Pyr/ β-CD)

2.4 Synthesis of Chs-Pyr/ZnO composite

Chs-Pyr polymer (1.0 g) and ZnO NPs (0.1g) were mixed in DMF (20ml) for 24 hours at room temperature to yield composite polymer, Scheme 3. It was produced as a yellow powder after the generated precipitate was filtered out under a vacuum and dried at room temperature.

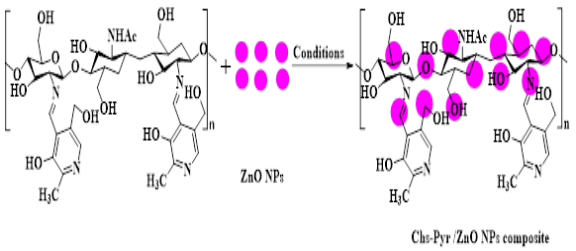

Scheme 3. Synthetic method for the preparation of Chs-Pyr/ZnO NPs composite

2.5 Characterizations

X-ray diffraction spectra were taken using a powder diffractometer (Brucker D8 Advance, Germany) with a Cu K radiation source, =1.5406 A, and 2 in the range (5-80°) to examine the phase structure and crystallite size of the materials. By employing an infrared spectrometer (Jasco Model 4100 - Japan) at room temperature, the chemical structures of the synthesized derivatives were investigated using FT-IR spectroscopy in the wave number range of 4000 - 400 cm1. Using an accelerated voltage of 10 kV, a scanning electron microscope (SEM) (JEOL SEM model JSM - 5500 - Japan) was used to examine the morphological structures of the produced derivatives. A UV-visible spectrometer was used to examine the produced polymers' optical characteristics. The UV-visible spectra were obtained using quartz cells with 1 cm path length and a UV-vis spectrophotometer (PG Instruments, model T80, UK) in the wavelength range of 270 to 600 nm. To change the baseline, DMF was utilized as a blank. The thermal stability of the synthesized derivatives was evaluated using TGA (SDT Q600 V20.9 Build 20, New castle, USA) at a heating rate of 15 °C/min up to 300 °C. 40 ml/min flow of nitrogen gas. The thermal analyzer has a data management and acquisition mechanism (TA-50WSI). The gas-sensing behavior of Chs-Pyr/ZnO NPs composite was accomplished utilizing a static homemade device comprising 5 L glass chamber and acquisition system containing digital multimeter interfaced laptop (Scheme 4) [27,28]. The sensor layer was fabricated by drop casting the composite suspension on interdigitated electrodes (5 cm×4 cm×2 cm) and allowed to dry for 24 h at 45 oC. The liquid analyte was injected in definite volumes to obtain the corresponding vapor concentrations [29]. The composite sensor's response was determined using the relation Ra / Rg, where Ra and Rg are the sensor's resistances in air and vapour, respectively [30]. The reaction and recovery times are the times required to achieve 90% of the final value [31].

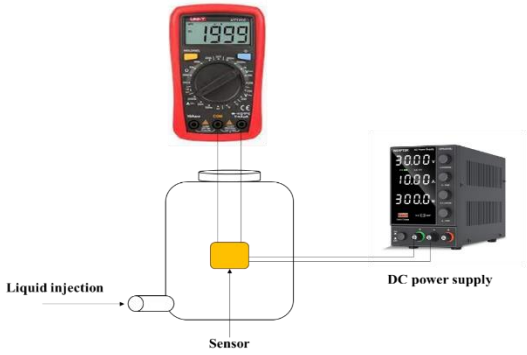

Scheme 4. Gas sensing setup

3. Results and discussion

3.1 XRD analysis

Chitosan, Chs-Pyr polymer, polymer composite, and pseudopolyrotaxane phase structures, crystallinity values and crystal sizes were determined and presented by XRD analysis Fig. 1. XRD examination Fig. 1 shows the XRD spectra obtained at 25 ºC in the range 5º−60º. Chitosan diffraction peaks were found at 8.6o and 20o, indicating its semi-crystalline structure due to hydrogen bonding

between hydroxyl, amino, and acetanilide groups [32]. XRD analysis for Chs-Pry polymer showed only one single broadening peak at 20.6° and slightly shifted from the chitosan peak. The pseudopolyrotaxane XRD pattern revealed a new peak at 11.8° and a small shift in 18.8°. Furthermore, increasing the intensity of the final peak increased the crystal size and crystallinity of pseudopolyrotaxane owing to hydrogen bonding between primary and secondary alcoholic -OH, which ascribed to β-CD cavity (Chs-Pyr /β-CD) polymer [33]. Chs-Pyr polymer and pseudopolyrotaxane have crystallinity values of 5% and 13%, respectively. In XRD examination, the addition of ZnO NPs to the Chs-Pyr polymer produced a distinct pattern. The Chs-Pyr/ZnO overseas peak became less intense and had distinct peaks at 28°, 31°, 35°, and 45°. The synthesis of these polymers was demonstrated by the change in XRD spectra of chitosan and other polymers.

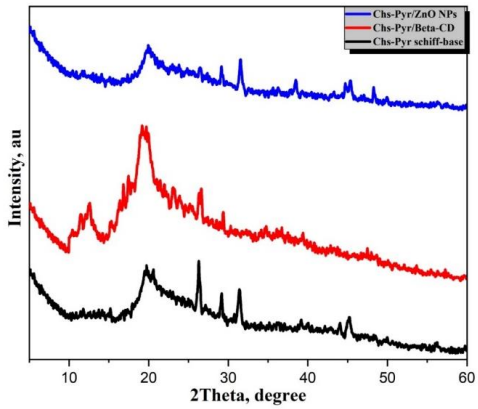

Fig. 1. XRD patterns of pure chitosan, Chs-Pyr polymer, Chs-Pyr/β-CD inclusion complex and Chs-Pyr ZnO NPs composite polymer.

3.2. Fourier-transform infrared spectroscopy (FT-IR)

The hydrocarbon bond C-H appeared at 2921 cm-1, and the -OH group characteristic peak in chitosan appeared at 3300 cm-1, superimposed over the N-H stretching band. In addition, the peaks of -C=O, amide, and –NH2 were observed at 1657 cm-1 and 1598 cm-1. FT-IR pattern of pure chitosan showed two transmission bands of asymmetric C-O-C and glucosamine C-O-C group at 1147 and 1071 cm-1, respectively, Table 1. The spectrum of Chs-Pyr polymer showed C=NH band at 1643 cm-1, these results confirmed the formation of Chs-Pyr after the condensation between the –NH2 of Chs and the C=O of Pyr, Scheme 1. The stretching vibration peaks of C-C bonds on the aromatic ring and the stretching vibration peak of C=O of Pyr appeared at 1490 and 1250 cm-1, respectively [34-36]. The differences between absorbance bands of chitosan and Chs-Pyr polymer are summarized in Table 1.

Additionally, the absorption band of the hydroxyl group in Chs-Pyr/ β-CD is slightly higher and more intense than the Chs-Pyr. Furthermore, the ν[C–O–C] and ν[CH2-O] bending vibrations were shifted to lower frequencies at 1050 and 1180 cm-1, respectively. Moreover, -C-H, -NH bands appeared at 2908 and 1580 cm-1, respectively. These results confirmed the formation of pseudopolyrotaxane polymer through the insertion of Chs-Pyr polymer into β-CD. Table 2 illustrates the differences in absorption bands between pure β-CD, Chs-Pyr polymer, and pseudopolyrotaxane polymer, respectively.

Table 1: Main functionalities of Ch and Chs-pyr obtained by FT-IR

Δν = ν (Chs-pyr polymer) – ν (Chs).

Functional group	Wavenumber, cm−1		Δν
	Chs	Chs-pyr polymer	
ν[OH, NH] symmetric	3334	3383	+49
ν[CH-aliphatic]	2978	2919	-59
ν[C=O]	1657	1617	-40
ν[C=N]	–	1569	-
ν[CH2-OH]	1378	1414	+36
ν[C-O-C]	1068	1074	+6

Table 2: Main functionalities of Chs-pyr, pseudopolyrotaxane, and β-CD obtained by FT-IR

Functional group	Δν3	Wavenumber, cm−1			Δν4
		Chs-pyr polymer	pseudopolyrotaxane	β-CD	
ν[OH, NH] symmetric	+12	3383	3395	3389	+6
ν[CH-aliphatic]	-11	2919	2908		-17
ν[C=O]	+36	1617	1653	2925	-
ν[CH2-OH]	-18	1414	1396	-	+237
ν[C-O-C]	+73	1074	1147	1159	+119
				1028	

Δν3 = ν (pseudopolyrotaxane) – ν (Chs-pyr polymer),

Δν4 = ν (pseudopolyrotaxane) – ν (β-CD

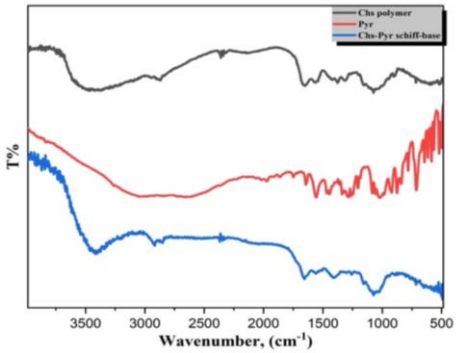

Fig. 2. FTIR spectra of pure chitosan (Chs) polymer, pyridoxal (Pyr) and Chs-Pyr Schiff-base polymer.

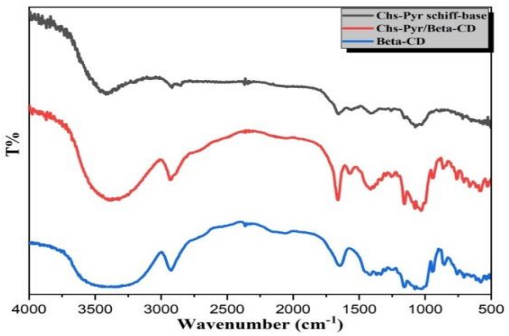

Fig. 3. FTIR spectra of pure β-CD, Chs-Pyr Schiff-base polymer and Chs-Pyr/ β-CD polymer.

The Chs-Pyr/ZnO composite polymer was formed by doping of Schiff-base with ZnO NPs. The FT-IR pattern of this polymer showed a broad absorption band at 3449 cm-1 corresponds to the stretching vibrations of hydroxyl (OH) groups. The absorption band located at 2888 cm-1 is attributed to symmetric stretching of aliphatic C–H groups of Chs in polymer blend [37], which is slightly shifted and decreased in intensity upon doping of ZnO NPs. The absorption band located at 1553 cm−1 is assigned to free C=O stretching vibration [38]. The absorption bands at 1606 and 1395 cm−1 corresponding to the polymer (C=N) group bending and stretching vibrations of the (CH2-OH) group were pushed towards higher wave numbers and decreased in intensity. The band at 1070 cm−1 is attributed to C–O-C stretching becoming less intense and shifted to a lower wavenumber. Furthermore, the band at 660 cm−1 reveals the presence of ZnO hexagonal phase in Chs-Pyr/ZnO composite polymer. The differences between the absorption bands of the Chs-pyr polymer and the Chs-Pyr/ ZnO NPs are summarized in Table 3.

Table 3
Main functionalities of Chs, Chs-pyr, Chs-pyr/ZnO NPs composite, and ZnO NPs obtained by FT-IR

Functional group	Δν1	Wavenumber, cm−1				Δν2
		Chs	Chs-pyr polymer	Chs-pyr/ZnO NPs composite	ZnO NPs	
ν[OH, NH] symmetric	+66	3334	3383	3449	3333	+11
ν[CH-aliphatic]	-31	2978	2919	2888	-	6
ν[C=O]	+10	1657	1617	1627	-	-
ν[NH-bending]	-18	–	1569	1551	1553	-2
ν[CH2-OH]	+16	1378	1414	1394	1395	-1
ν[C-O-C]	+3	1068	1074	1079	1090	-11

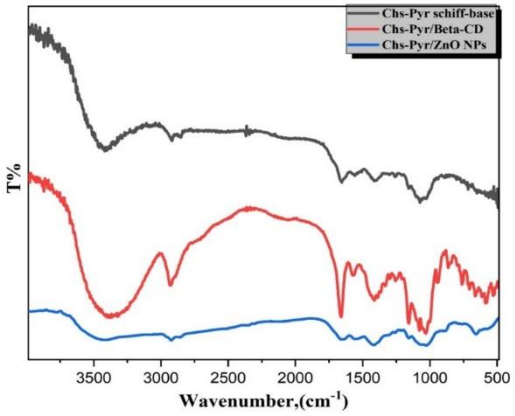

Δν1 = ν (Chs-pyr/ZnO NPs) – ν (Chs-pyr polymer), Δν2 = ν (Chs-pyr/ZnO NPs) – ν (ZnO NPs).

Fig. 4. FTIR spectra of all prepared polymers

3.3. SEM measurement

Chitosan, pyridoxal aldehyde, Chs-Pyr polymer, pesedopolyrotaxane, ZnO NPS, and composite polymer's morphological structures were analyzed using SEM (Fig. 5 a-f). Pure chitosan is exceedingly homogeneous, level, normal, and smooth, without any pores or fissures (Fig. 5-a). SEM analysis revealed the morphological structure of the Chs-Pyr polymer as a black, uniform, and dense clouds with few corrugations and no fissures. (Fig. 5-c), and the surface pyridoxal aldehyde is very smooth with a tiny grey rock [39]. The morphological structure of pesedopolyrotaxane (Fig. 5-d) cite to snowflakes of β-CD coated gray clouds polymer indicates the penetration of Schiff-base polymer into β-CD, while (Fig. 5-e) alludes to morphological arrangement of pure ZnO NPs which developed on coral reefs. Ergo Chs-Pyr and ZnO NPS morphological organization appears as an ice cube on the cloudy skies belonging to Chs-Pyr polymer's surface (Fig. 5-f).

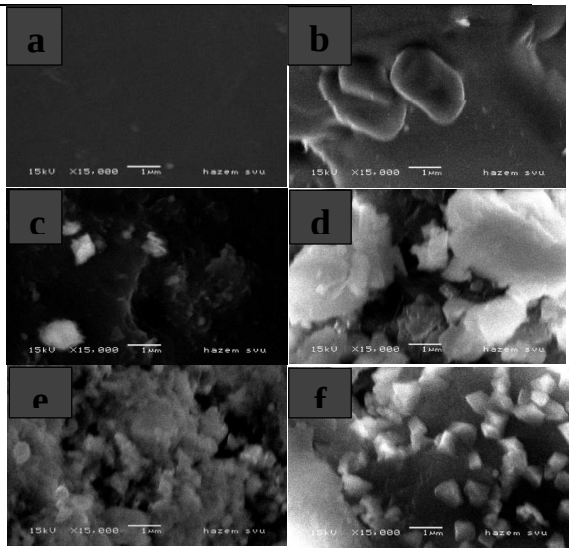

Fig. 5. SEM images of a) Pure Chitosan, b) pyridoxal, c) Ch-Pyr, d) Chs-Pyr/ βCD, e) ZnO NPs and f) Chs-Pyr / ZnO NPs

3.4. Optical analysis

UV-visible spectroscopy of the Chs-Pyr polymer, Chs-Pyr/β-CD polymer, Chs-Pyr/ZnO NPs composite and chitosan were observed to be in the range of 225–600 nm at 25 °C. Fig. 6. The characteristic peak of chitosan appears at wavelength 280 nm due to the transition of the electrons which staying in the carbonyl group (>C=O) by π- $\pi*$ transition. The Chs-Pyr polymer recorded the very broading band at 292 nm due to presence of π bond in Schiff-base (-CH=N-). The modification of Chs-Pyr polymer with β-CD leads to the absorption peak rang change from 292 nm to 296 nm, this red shift due to hydroxyl groups which are present in β-CD. When ZnO NPs were added to the Chs-Pyr polymer, shifted (red shift) and very broad peak at wavelength 297 nm. All the shifted values indicated the formation of Chs-Pyr polymer, Chs-Pyr/β-CD polymer and Chs-Pyr/ZnO NPs composite. Furthermore, using Tauc's formula, the

energy gap of the synthesized polymers was computed based on the UV-visible absorption spectra. For the Chs-Pyr polymer, Chs-Pyr/β-CD polymer, and Chs-Pyr/ZnO NPs composite, the corresponding values of Eg were 2.95 ev, 3.03 ev, and 3.09 ev.

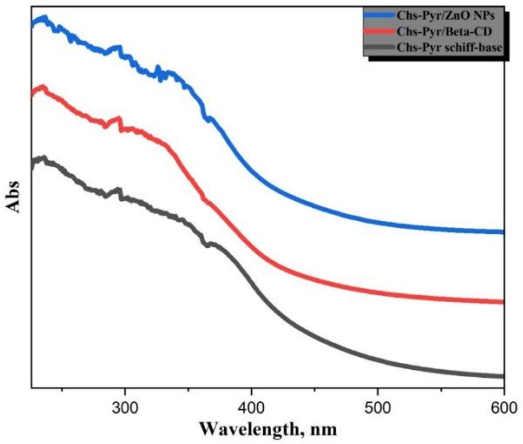

Fig. 6. UV-vis spectral of all prepared polymer

3.5. Thermal analysis (TGA)

The TG-DTG analysis in the temperature range of 20 to 600 °C under nitrogen (N2) environment was utilized as a straightforward, affordable, and accurate analysis. The temperature range and three different weight loss phases were observed in the Chs-pyr TG curve. Due to the hydrophilicity of the chitosan molecule, the first weight loss reflects the removal of water molecules that were physically associating with the Schiff-base polymer. However, the following stage of loss of weight involves the decomposition of glycosidic bonds along the Chs-Pyr chain, the breakdown of amino groups, and depolymerization. In addition, the third weight loss phase involves the breaking down of saccharide units, the disintegration of condensed chitosan units, and the disbandment of pyridoxal rings. Differential thermal analysis provided additional details regarding the stages of thermal deterioration of the polymers (DTG). It was observed that Chs-Pyr polymer modifications that involved encapsulating it in β-CD hydrophobic cavity and coordinating it with ZnO NPs resulted in a comparatively increased thermal stability of the Schiff base. T50 provided confirmation of these findings. (The temperature at which the polymers lose half of their weight). T50 was determined to be 271, 291, and 299.8 C for Chs-Pyr Schiff base, Chs-Pyr/-CD, and Chs-Pyr/ZnO NPs, respectively.

3.6 Gas sensing performance

(Fig. 8A) represent the dynamic response of the polymer composite sensor towards different NH3 concentrations at room temperature. The prepared Chs-Pyr/ β-CD/ZnO NPs polymer composite gained high sensitivity for NH3 from 10 to 100 ppm. It was observed that the resistance of the sensor was decreased by increasing concentration of the NH3 analyte, and then recovered again by removing the analyte vapor, as an indication of reversible response characteristics. Also, the response of the composite sensor was increased as NH3 concentration was increased (Fig. 8B, 8C).

As the bulky Schiff base polymer has a porous structure, it may provide efficient sensing properties. Pyridoxal has bulky structure, which make globular head in Schiff base that provides porosity and sufficient space for adsorption of vapor leading to high sensitivity of the prepared Chs-Pyr/ β-CD/ZnO composite [40]. On one hand, ZnO NPs-based sensor play important rule in NH3 vapor sensing due to adsorption–desorption process of the reducing NH3 gas on the surface of ZnO NPs which decreasing the resistance of the sensor according to the mechanism reported by Anshika Nagar *et. al* [7]. The sensor response and recovery times were 589 s and 264 s, respectively (Fig. 8D) indicating that Chs-Pyr / β-CD/ZnO NPs composite is suitable for gas sensing applications [27].

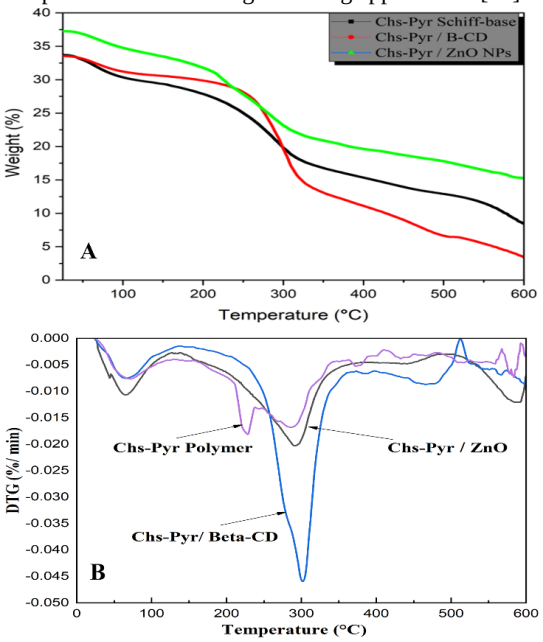

Fig. 7. (A) and (B): TGA and DTG diffractograms of all prepared polymers.

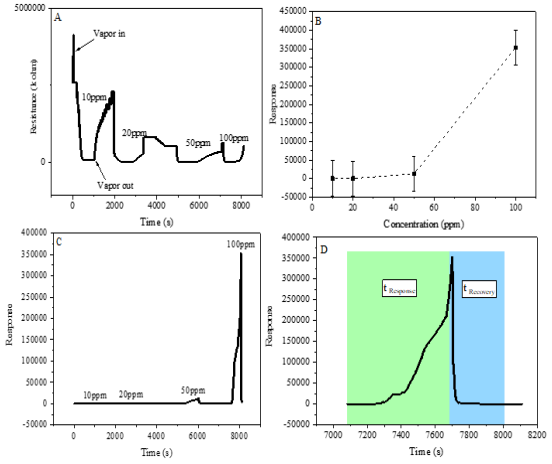

Fig. 8. Dynamic response of Chs-Pyr / β-CD/ZnO NPs composite toward different NH3 concentrations (A), maximum response of the composite different NH3 concentrations (B), Sensing response versus different NH3 concentrations (C), and response and recovery times of the composite at 100 ppm NH3 (D)

Conclusions

Chitosan was reacted with pyridoxal to afford Chs-Pyr polymer. By modification of Chs-Pyr polymer via insertion it into β-CD and doping it with ZnO NPs gave Chs-Pyr/β-CD polymer and Chs-Pyr/ZnO NPs, respectively. All these polymers were characterized by XRD, FT-IR, TGA, SEM analysis and optical analysis and the Chs-Pyr/ZnO composite was tested as toxic vapors. The formation of porous structure in the Chs-Pyr/ZnO composite provides sufficient molecular space to facilitate housing of the analyte molecules and resulting high vapor sensitivity. The Chs-Pyr/ ZnO composite was evaluated as a sensor for aliphatic amine vapor, such as ammonia at room temperature in concentrations ranging from 10 ppm to 100 ppm. The composite is effective for detecting NH3 vapors with quick response and recovery time indicating that the composite can be utilized in toxic vapors sensing devices.

Conflicts of interest

The authors declare that they have no known competing financial interest or personal relationships that could have appeared to influence the work reported in.

References

. [1] Wang, Z., Su, J., Ali, A., Yang, W., Zhang, R., Li, Y., Zhang, L., Li, J. (2022). Chitosan and carboxymethyl chitosan mimic biomineralization and promote microbially induced calcium precipitation. Carbohydrate Polymers, 287, 119335.

. [2] Gulzar, S., Raju, N., Prodpran, T., & Benjakul, S. (2022). Chitosan-tripolyphosphate nanoparticles improves oxidative stability of encapsulated shrimp oil throughout the extended storage. European Journal of Lipid Science and Technology, 124(1), 2100178.

[3] Ke, Y., Ding, B., Zhang, M., Dong, T., Fu, Y., Lv, Q., Ding, W., & Wang, X. (2022). Study on inhibitory activity and mechanism of chitosan oligosaccharides on Aspergillus Flavus and Aspergillus Fumigatus. Carbohydrate Polymers, 275, 118673.

[4] Karimi, F., Ayati, A., Tanhaei, B., Sanati, A. L., Afshar, S., Kardan, A., Dabirifar, Z., & Karaman, C. (2022). Removal of metal ions using a new magnetic chitosan nano-bio-adsorbent; A powerful approach in water treatment. Environmental Research, 203, 111753.

[5] Garavand, F., Cacciotti, I., Vahedikia, N., Rehman, A., Tarhan, Ö., Akbari-Alavijeh, S., Shaddel, R., Rashidinejad, A., Nejatian, M., Jafarzadeh, S., Azizi-Lalabadi, M., Khoshnoudi-Nia, S., & Jafari, S. M. (2022). A comprehensive review on the nanocomposites loaded with chitosan nanoparticles for food packaging. Critical Reviews in Food Science and Nutrition, 62(5), 1383–1416.

[6] Furlani, F., Rossi, A., Grimaudo, M. A., Bassi, G., Giusto, E., Molinari, F., Lista, F., Montesi, M., & Panseri, S. (2022). Controlled liposome delivery from chitosan-based thermosensitive hydrogel for regenerative medicine. International Journal of Molecular Sciences, 23(2), 894.

[7] Mondéjar-López, M., López-Jimenez, A. J., García Martínez, J. C., Ahrazem, O., Gómez-Gómez, L., & Niza, E. (2022). Comparative evaluation of carvacrol and eugenol chitosan nanoparticles as eco-friendly preservative agents in cosmetics. International Journal of Biological Macromolecules, 206, 288–297.

[8] Fidalgo, D. M., Agusti, R., & D'Accorso, N. B. (2022). Enzyme immobilization using chitosan systems. In Chitosan in Biomedical Applications (pp. 273–294). Elsevier.

[9] Zhang, M., Zhang, F., Li, C., An, H., Wan, T., & Zhang, P. (2022). Application of chitosan and its derivative polymers in clinical medicine and agriculture. Polymers, 14(5), 958.

[10] Hamed, A. A., Saad, G. R., Abdelhamid, I. A., Elwahy, A. H. M., Abdel-Aziz, M. M., & Elsabee, M. Z. (2022). Chitosan Schiff bases-based polyelectrolyte complexes with graphene quantum dots and their prospective biomedical applications. International Journal of Biological Macromolecules, 208, 1029–1045.

[11] Huang, X., Liu, Y., Liu, S., Tan, X., Ding, Y., Zeng, G., Zhou, Y., Zhang, M., Wang, S., & Zheng, B. (2016). Effective removal of Cr (VI) using β-cyclodextrin–chitosan modified biochars with adsorption/reduction bifuctional roles. RSC Advances, 6(1), 94–104.

[12] Turza, A., Borodi, G., Muresan-Pop, M., & Ulici, A. (2022). Polymorphism and β-cyclodextrin complexation of methyldrostanolone. Journal of Molecular Structure, 1250, 131852.

[13] Cid-Samamed, A., Rakmai, J., Mejuto, J. C., Simal-Gandara, J., & Astray, G. (2022). Cyclodextrins inclusion complex: Preparation methods, analytical techniques, and food industry applications. Food Chemistry, 384, 132467.

[14] Deng, C., Cao, C., Zhang, Y., Hu, J., Gong, Y., Zheng, M., & Zhou, Y. (2022). Formation and stabilization mechanism of β-cyclodextrin inclusion complex with C10 aroma molecules. Food Hydrocolloids, 123, 107013.

[15] Lin, Y., Huang, R., Sun, X., Yu, X., Xiao, Y., Wang, L., Hu, W., & Zhong, T. (2022). The p-Anisaldehyde/β-cyclodextrin inclusion complexes as a sustained release agent: Characterization, storage stability, antibacterial and antioxidant activity. Food Control, 132, 108561.

[16] Tommalieh, M. J., Ibrahium, H. A., Awwad, N. S., & Menazea, A. A. (2020). Gold nanoparticles doped Polyvinyl Alcohol/Chitosan blend via laser ablation for electrical conductivity enhancement. Journal of Molecular Structure, 1221, 128814.

[17] Morsi, M. A., Rajeh, A., & Menazea, A. A. (2019). Nanosecond laser-irradiation assisted the improvement of structural, optical, and thermal properties of polyvinyl pyrrolidone/carboxymethyl cellulose blend filled with gold nanoparticles. Journal of Materials Science: Materials in Electronics, 30(3), 2693–2705.

[18] Elashmawi, I. S., & Elsayed, N. H. (2020). The role of gold nanoparticles in the structural and electrical properties of Cs/PVP blend. Polymer Bulletin, 77(2), 949–962.

[19] Ahmed, M. K., Ramadan, R., Afifi, M., & Menazea, A. A. (2020). Au-doped carbonated hydroxyapatite sputtered on alumina scaffolds via pulsed laser deposition for biomedical applications. Journal of Materials Research and Technology, 9(4), 8854–8866.

[20] Ahmad, M. Z., Rizwanullah, Md., Ahmad, J., Alasmary, M. Y., Akhter, Md. H., Abdel-Wahab, B. A., Warsi, M. H., & Haque, A. (2022). Progress in nanomedicine-based drug delivery in designing of chitosan nanoparticles for cancer therapy. International Journal of Polymeric Materials and Polymeric Biomaterials, 71(8), 602–623.

[21] Cao, S., Deng, Y., Zhang, L., & Aleahmad, M. (2022). Chitosan nanoparticles, as biological macromolecule-based drug delivery systems to improve the healing

potential of artificial neural guidance channels: A review. International Journal of Biological Macromolecules, 201, 569–579.

[22] Hosseini, S. M., Mazinani, S., Abdouss, M., Kalhor, H., Kalantari, K., Amiri, I. S., & Ramezani, Z. (2022). Designing chitosan nanoparticles embedded into graphene oxide as a drug delivery system. Polymer Bulletin, 79(1), 541–554.

[23] Garavand, F., Cacciotti, I., Vahedikia, N., Rehman, A., Tarhan, Ö., Akbari-Alavijeh, S., Shaddel, R., Rashidinejad, A., Nejatian, M., Jafarzadeh, S., Azizi-Lalabadi, M., Khoshnoudi-Nia, S., & Jafari, S. M. (2022). A comprehensive review on the nanocomposites loaded with chitosan nanoparticles for food packaging. Critical Reviews in Food Science and Nutrition, 62(5), 1383–1416.

[24] Suginta, W., Khunkaewla, P., & Schulte, A. (2013). Electrochemical biosensor applications of polysaccharides chitin and chitosan. Chemical Reviews, 113(7), 5458–5479.

[25] Lu, G., Yao, X., Wu, X., & Zhan, T. (2001). Determination of the total iron by chitosan-modified glassy carbon electrode. Microchemical Journal, 69(1), 81–87.

[26] Xin, Y., Guanghan, L., Xiaogang, W., & Tong, Z. (2001). Studies on electrochemical behavior of bromideat a chitosan-modified glassy carbon electrode. Electroanalysis, 13(11), 923–926.

[27] S. Dacrory, A.M. Saeed, R.E. Abouzeid, A novel ammonia sensor based on cellulose/graphene oxide functionalized with ethylenediamine, Express Polym. Lett. 16 (2022) 786–797.

[28] A. Fahmy, A.M. Saeed, U. Dawood, H. Abdelbary, K. Altmann, A. Schönhals, Nano-MnO2/xanthan gum composite films for NO2 gas sensing, Mater. Chem. Phys. 296 (2023) 127277.

[29] G. Fan, D. Chen, T. Li, S. Yi, H. Ji, Y. Wang, Z. Zhang, G. Shao, B. Fan, H. Wang, H. Xu, H. Lu, Y. Zhou, R. Zhang, J. Sun, Enhanced room-temperature ammonia-sensing properties of polyaniline-modified WO3 nanoplates derived via ultrasonic spray process, Sensors Actuators, B Chem. 312 (2020).

[30] X. Qiang, M. Hu, B. Zhao, Y. Qin, T. Zhang, L. Zhou, J. Liang, Preparation of porous silicon/Pd-loaded WO3 nanowires for enhancement of ammonia sensing properties at room temperature, Mater. Sci. Semicond. Process. 79 (2018) 113–118.

[31] G.J. Thangamani, S.K.K. Pasha, Titanium dioxide (TiO2) nanoparticles reinforced polyvinyl formal (PVF) nanocomposites as chemiresistive gas sensor for sulfur dioxide (SO2) monitoring, Chemosphere. 275 (2021) 129960.

[32] Elhag, M., Abdelwahab, H. E., Mostafa, M. A., Yacout, G. A., Nasr, A. Z., Dambruoso, P., & El Sadek, M. M. (2021). One pot synthesis of new cross-linked chitosan-Schiff' base: Characterization, and anti-proliferative activities. International Journal of Biological Macromolecules, 184, 558–565.

[33] Anuradha, Kumari, S., Layek, S., & Pathak, D. D. (2017). Chitosan supported Zn (II) mixed ligand complexes as heterogeneous catalysts for one-pot synthesis of amides from ketones via Beckmann rearrangement. Journal of Molecular Structure, 1130, 368–373.

[34] Huang, C., Liao, H., Ma, X., Xiao, M., Liu, X., Gong, S., Shu, X., & Zhou, X. (2021). Adsorption performance of chitosan Schiff base towards anionic dyes: Electrostatic interaction effects. Chemical Physics Letters, 780, 138958.

[35] Ansari, K. R., Chauhan, D. S., Quraishi, M. A., Mazumder, M. A. J., & Singh, A. (2020). Chitosan Schiff base: an environmentally benign biological macromolecule as a new corrosion inhibitor for oil & gas industries. International Journal of Biological Macromolecules, 144, 305–315.

[36] Guinesi, L. S., & Cavalheiro, É. T. G. (2006). Influence of some reactional parameters on the substitution degree of biopolymeric Schiff bases prepared from chitosan and salicylaldehyde. Carbohydrate Polymers, 65(4), 557–561.

[37] Khowdiary, M. M., El-Henawy, A. A., Shawky, A. M., Sameeh, M. Y., & Negm, N. A. (2017). Synthesis, characterization, and biocidal efficiency of quaternary ammonium polymers silver nanohybrids against sulfate reducing bacteria. Journal of Molecular Liquids, 230, 163–168.

[38] Abdelrazek, E. M., Elashmawi, I. S., Hezma, A. M., Rajeh, A., & Kamal, M. (2016). Effect of an encapsulate carbon nanotubes (CNTs) on structural and electrical properties of PU/PVC nanocomposites. Physica B: Condensed Matter, 502, 48–55.

[39] Dardeer, H. M., Abbas, S. A., El-Sayyad, G. S., & Ali, M. F. (2022). Effect of titanium dioxide nanoparticles and β-cyclodextrin polymer on physicochemical, antimicrobial, and antibiofilm properties of a novel chitosan-camphor polymer. International Journal of Biological Macromolecules, 219, 1062–1079.

[40] R. Das, R. Bandyopadhyay, P. Pramanik, Stereo-regulated Schiff base siloxane polymer coated QCM sensor for amine vapor detection, Mater. Chem. Phys. 226 (2019) 214–219.

[41] A. Nagar, A. Kumar, U. Tyagi, H. Dhasmana, M.A.M. Khan, S. Husain, A. Verma, V.K. Jain, Ultrafast, trace-level detection of NH3 gas at room temperature using hexagonal-shaped ZnO nanoparticles grown by novel green synthesis technique, Phys. B Condens. Matter. 626 (2022) 413595.

[